Estimates of Potential Vorticity at Small Scales in the Ocean

PETER MÜLLER, REN-CHIEH LIEN AND ROBIN WILLIAMS*

Department of Oceanography, Hawaii Institute of Geophysics, University of Hawaii, Honolulu, Hawaii

(Manuscript received 30 April 1987, in final form 10 September 1987)

ABSTRACT

The trimoored design of the current meter array of the Internal Wave Experiment (IWEX) is exploited to calculate time series of relative vorticity, horizontal divergence, vortex stretching, and (linear) potential vorticity at five different levels in the vertical. Potential vorticity characterizes the vortical mode of motion which coexists with the (internal) gravity mode (which does not carry potential vorticity). The amplitudes, and the space- and time-scales of the vortical mode, or potential vorticity field, are determined by spectral analysis. The observed variance of potential vorticity (enstrophy) is 10^{-6} s^{-2}, implying a Rossby number of order 10, the energy 2 $\times 10^{-4}$ m^2 s^{-2} and the inverse Richardson number 0.7. The observed frequencies are interpreted as Doppler frequencies. A low frequency "steppy" potential vorticity field is advected vertically past the sensors by internal gravity waves. The advected potential vorticity field is characterized by a vertical wavenumber smaller than 0.2 m^{-1} and by a +2/3 (enstrophy) or −4/3 (energy) power law with respect to horizontal wavenumber. These results are summarized in a model wavenumber–frequency spectrum. The results indicate that vortical or potential vorticity carrying motion exists at scales traditionally associated with internal gravity waves and that these small-scale vortical motions contribute significantly to the observed shear.

1. Introduction

Traditionally, all oceanic motions in the frequency band between the Coriolis and Brunt–Väisälä frequency have been attributed to internal gravity waves. However, internal gravity waves do not provide a complete description of the motions in an incompressible Boussinesq fluid. (The term "Boussinesq" refers here to a fluid whose dynamical evolution is determined by density and not by the individual temperature and salinity fields. Such fluids do not exhibit double diffusion, cabbeling and other two-component effects.) The fluid does support three modes of motion. Two modes represent internal gravity waves. The third mode represents an entirely different type of motion. In a linear f-plane analysis this third mode is the zero-frequency mode describing steady horizontal geostrophic flows. The three eigenvectors of the linear problem can be used to decompose any observed velocity and density field. The decomposition is unique and complete at any scale. The algebra is briefly outlined in appendix A. In such a modal decomposition, the distinguishing property of the third mode is that it carries potential vorticity while internal gravity waves do not. Potential vorticity is here defined as

$$\mathrm{PV} = f + (\partial_x v - \partial_y u) - f\partial_z \xi \qquad (1)$$

where x, y and z are right-handed Cartesian coordinates with z positive upwards, u and v the horizontal velocity components, f the Coriolis frequency, and ξ the vertical displacement. The first term represents planetary vorticity, the middle term relative vorticity, and the last term vortex stretching. The potential vorticity PV, defined in (1) is a linearized version of Ertel's (1942) potential vorticity

$$\pi = (\mathbf{f} + \nabla \times \mathbf{u}) \cdot \nabla(z - \xi) \qquad (2)$$

which is conserved for inviscid and adiabatic motions.

At large- and mesoscales the third (or potential vorticity carrying) mode is in geostrophic and hydrostatic balance, is horizontally nondivergent, and satisfies the thermal wind relations. It is therefore the usual geostrophic mode. This mode also exists at small scales and in the nonrotating case and need not be in geostrophic balance. To include such cases this mode has been termed "vortical" (instead of geostrophic) by Müller et al. (1986), to emphasize its defining property of having nonzero potential vorticity.

The decomposition of an incompressible Boussinesq flow into its three eigenmodes is a standard operation and has long been recognized. At small scales, the existence of the vortical mode has, however, been ignored, presumably for four reasons:

* Present affiliation: Scott Polar Research Institute, Cambridge, England.

Corresponding author address: Dr. Peter Müller, University of Hawaii at Manoa, Department of Oceanography, Division of Natural Sciences, 1000 Pope Road, Honolulu, Hawaii 96822.

- In a linear analysis, the vortical mode has zero frequency (on an f-plane) and was therefore assumed to be a large scale phenomenon.
- Most nonlinear interaction calculations (recently reviewed by Müller et al., 1986) intrinsically exclude the vortical mode: Lagrangian studies because perturbations are assumed proportional to $\exp\{i\omega t\}$ and numerical studies by confining themselves to motions in a nonrotating vertical plane. The only three-dimensional numerical study (Riley et al., 1981) did find small-scale potential vorticity.
- The lack of any obvious dynamical balance for such motions. Small-scale vortical motions are not in geostrophic but presumably in cyclostrophic balance (where pressure gradients are balanced by the nonlinear acceleration terms). A complete dynamical balance of such high Rossby number flows has only been worked out in the high Richardson number (low Froude number) limit and termed "two-dimensional stratified turbulence" (Riley et al., 1981; Lilly, 1983). A Richardson number of order one is more appropriate for realistic oceanic conditions.
- Potential vorticity has yet to be measured at small scales, a point we will attempt to remedy in this paper.

Interest in the vortical mode comes from many sides. In going beyond weak resonant interactions, theoreticians are forced to carry out a normal mode decomposition of the incompressible Boussinesq equations that includes the vortical mode (e.g., Holloway, 1981, 1983; Riley et al., 1981; Henyey, 1983; Müller, 1984). On the observational side, there are indications that the observed variance in the frequency band between the Coriolis frequency f and the Brunt–Väisälä frequency N cannot be attributed to internal gravity waves alone:

- Horizontal kinetic energy spectra exhibit levels which are higher than those inferred from vertical displacement spectra by internal wave theory (e.g., Briscoe, 1975; Eriksen, 1978; Pinkel, 1985).
- Horizontal kinetic energy occurs at frequencies greater than the local Brunt–Väisälä frequency.
- The vertical coherence between horizontal currents is smaller than between vertical displacements.

All these discrepancies indicate that there exists some excess horizontal kinetic energy that is not consistent with linear internal wave theory. Indeed, in their inverse analysis of the IWEX data Mülller et al. (1978) were forced to introduce additional signals, "current finestructure" and "current noise", in order to arrive at a consistent quantitative interpretation. Intensity and vertical coherence scale of current finestructure were also estimated by Briscoe (1977). To further understand the nature of current finestructure, and other excess energies, is the motivation for the present paper.

Interest in small-scale vortical motions has also been stimulated by research in meteorology where the situation is just reversed. The mesoscale part of the atmospheric spectrum is generally interpreted as two-dimensional stratified turbulence, i.e., as vortical motion (e.g., Gage, 1979; Lilly, 1983). Only recently have there been attempts to interpret it as internal gravity waves (Van Zandt, 1982).

At present, it is unknown to what extent the vortical mode is excited at small scales, what its energy and shear content is, and how it is generated and dissipated. As a first step towards answering these questions we estimate the amplitudes, and the space and time scales of relative vorticity, horizontal divergence, vortex stretching and potential vorticity from the IWEX dataset. This particular dataset is chosen because the trimoored design of IWEX permits estimation of all these quantities from the current meter array alone, without recourse to displacement estimates which are contaminated by temperature finestructure (Joyce and Desaubies, 1977). We will first review the configuration of the IWEX mooring, explain our technique for estimating potential vorticity, and discuss sampling and measurement errors. The latter point needs elaboration since we difference current measurements. We then determine the space and time scales of potential vorticity and suggest a model wavenumber–frequency spectrum. A summary of our results and a discussion of the main problems is given in the last section. The major point to keep in mind is that we measure and discuss the linear potential vorticity PV, as defined in (1), and not Ertel's potential vorticity.

2. IWEX

IWEX (Internal Wave Experiment) was performed for 42 days at a site (27°44′N, 69°51′W) in the Sargasso Sea. An extremely stable three-legged mooring in the form of a tetrahedron supported current meters on eight horizontal levels between 604 and 2050 m. Figure 1 illustrates the geometry of the array and displays profiles of the Brunt–Väisälä frequency $N(z)$ and the horizontal radius R of the current meter triangles. Except for the deepest level the current meter were VACMs (vector averaging current meters) which sampled every 225 s. At the deepest level EG & G 850 current meters were deployed with a 900 s sampling interval. Further details of the experiment and its preliminary analysis are described in Briscoe (1975), and the results of a rigorous inverse analysis are given in Müller et al. (1978).

Our analysis requires three current meters on a horizontal level. There are five such levels, level 2, 5, 6, 10 and 14. Some pertinent characteristics of these levels are summarized in Table 1. Note that all these levels, except for the deepest one, lie in the main thermocline where the Brunt–Väisälä frequency is nearly constant, within 15% of $N = 2.4$ cph. Time series of temperature and temperature difference were also recorded at each current meter, but are not used here for the reason given above.

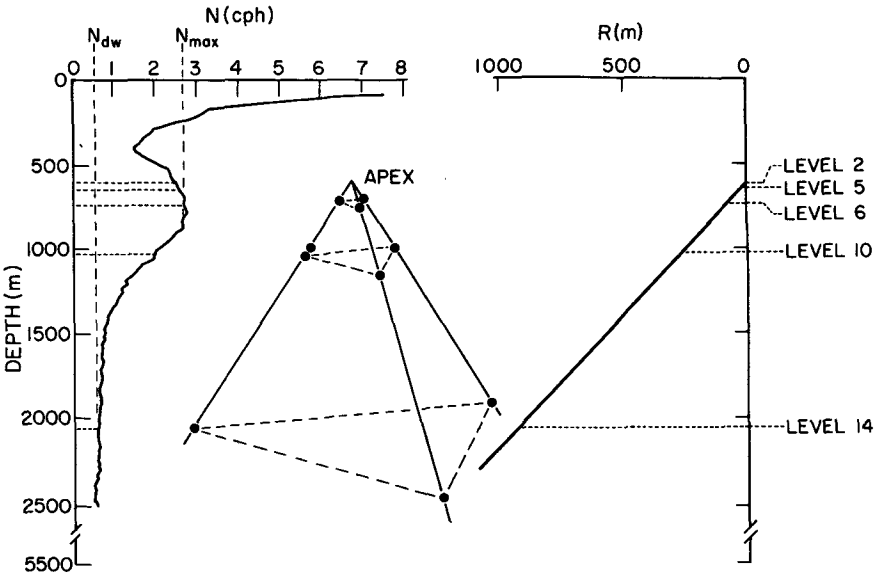

FIG. 1. Schematic view of the geometry of the IWEX array and profiles of the Brunt–Väisälä frequency $N(z)$ and horizontal radius $R(z)$. Points indicate current meter positions. There are ten more current meters near the apex which are not shown. The levels that contain three current meters are indicated. The maximum Brunt–Väisälä frequency in the main thermocline is N_{max} = 2.76 cph. In the deep water column below 2050 m N is almost constant, N_{dw} = 0.36 cph.

3. Data analysis

At each level with current meters on all three legs, one can estimate the area-averaged values of relative vorticity RV and horizontal divergence HD by using Stokes' and Gauss' theorem

$$\overline{\mathrm{RV}} = \frac{1}{A}\int dA(\partial_x v - \partial_y u) = \frac{1}{A}\oint \mathbf{u}\cdot d\mathbf{t} \qquad (3a)$$

$$\overline{\mathrm{HD}} = \frac{1}{A}\int dA(\partial_x u + \partial_y v) = \frac{1}{A}\oint \mathbf{u}\cdot d\mathbf{n}. \qquad (3b)$$

Here **t** is the tangential and **n** the normal unit vector along the circumference and A the area of the circle connecting the three current meters. The line integrals can be approximated by decomposing the three observed velocities into normal and tangential components. Since the three current meters form an equilateral triangle, the explicit formulas are

$$\overline{\mathrm{RV}} = \frac{1}{\pi R^2}\sum_{k=A,B,C}\{v_k\cos(\theta+\phi_k) - u_k\sin(\theta+\phi_k)\}\frac{2\pi R}{3} \qquad (4a)$$

$$\overline{\mathrm{HD}} = \frac{1}{\pi R^2}\sum_{k=A,B,C}\{v_k\sin(\theta+\phi_k) + u_k\cos(\theta+\phi_k)\}\frac{2\pi R}{3} \qquad (4b)$$

TABLE 1. Characteristics of the five IWEX levels that contain three current meters.

Level	Depth (m)	Horizontal separation (m)	Radius (m)	Cutoff wavenumber (m^{-1})	N (cph)	N/f	Record length	Number of points	Rms vertical displacement (m)**
2	606	8.5	4.9	3.5×10^{-1}	2.54	65	4 d 16.5 h	1 800	6.9
5	640	44.0	25.4	6.7×10^{-2}	2.60	67	31 d 6 h	12 000	6.8
6	731	139	80.3	2.1×10^{-2}	2.76	71	31 d 6 h	12 000	6.4
10	1 023	450	260	6.5×10^{-3}	2.05	53	12 d 12 h*	4 800*	8.6
							+12 d 12 h	4 800	
14	2 050	1 600	925	1.8×10^{-3}	0.66	17	40 d 15 h	3 900	26.7

* Good data consist of two disjunct pieces.

** rms values have been estimated from measured value at level 4 (Joyce and Desaubies, 1977) and WKB scaling to other levels.

where u_k and v_k are the east and north components of velocity at the three legs $k = A, B$ and C, $\theta = \pi/3$ the orientation of the array, and $\phi_k = 4\pi/3, 2\pi/3, 0$ for $k = A, B, C$. Using the incompressibility condition, $\partial_z w = -(\partial_x u + \partial_y v)$ and $\partial_t \xi = w$, we can also estimate the area-averaged values of vertical strain

$$\overline{\partial_z \xi} = \int dt\, \overline{\partial_z w} = -\int dt \overline{\mathrm{HD}} \tag{5}$$

vortex stretching

$$\overline{\mathrm{VS}} = -f\overline{\partial_z \xi} \tag{6}$$

and potential vorticity

$$\overline{\mathrm{PV}} = \overline{\mathrm{RV}} + \overline{\mathrm{VS}}. \tag{7}$$

The estimate of the vertical strain involves a linearization since the exact relationship between vertical displacement and vertical velocity is $D\xi/Dt = w$, where D/Dt is the advective derivative. The linearization is justified as long as the strains are smaller than one.

Using (4) through (7), time series of $\overline{\mathrm{RV}}(t)$, $\overline{\mathrm{HD}}(t)$, $\overline{\mathrm{VS}}(t)$ and $\overline{\mathrm{PV}}(t)$ are calculated. Figure 2 shows these time series for level 6. The time series at the other levels look similar, except for a systematic decrease in overall amplitude with depth.

Spectra of the time series are calculated in the following way. Fifty percent overlapping 75 hour-long subsections of the time series are first subjected to a Hanning window and then fast Fourier transformed. From the transforms, one-sided spectra are calculated. These spectra are piece and frequency averaged to yield estimates at 40 frequency points spaced about equally on a logarithmic frequency axis. Coherence between time series at different levels are also calculated. These spectra and coherences form the basis for estimating the amplitude and the space- and time-scales of potential vorticity and its components. The time series, means, variances, spectra, and coherences are fully documented in a technical report by Williams and Müller (1986).

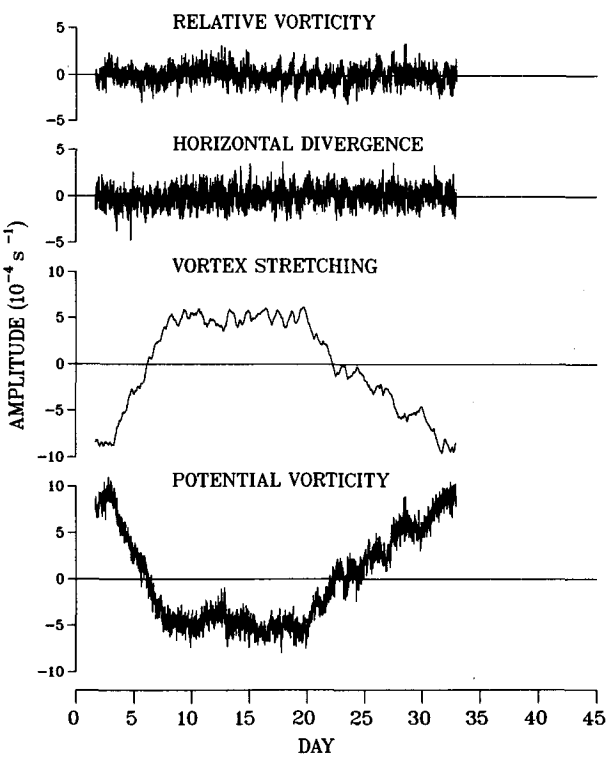

FIG. 2. Time series (mean removed) of area-averaged relative vorticity, horizontal divergence, vortex stretching and potential vorticity at level 6. The time series are 31 d 6 h long and consist of 12 000 points each.

4. Sampling errors

Gradients of velocity are very sensitive to sampling and measurement errors. Sampling errors arise because the averaged value of relative vorticity and horizontal divergence are not calculated from the continuous line integral but from three discrete locations. If $S_{\mathrm{RV}}(\alpha, \omega)$ represents the horizontal wavenumber–frequency spectrum of relative vorticity, then the frequency spectrum of the area-averaged relative vorticity

$$\overline{\mathrm{RV}} = \frac{1}{\pi R^2}\int d^2x \mathrm{RV}$$

is given by

$$S_{\overline{\mathrm{RV}}}(\omega) = \int d\alpha F_c(\alpha) S_{\mathrm{RV}}(\alpha, \omega) \tag{8}$$

with the filter

$$F_c(\alpha) = \frac{4J_1^2(\alpha R)}{(\alpha R)^2}. \tag{9}$$

Here J_1 is the Bessel function of the first kind of the first order. If the frequency spectrum of $\overline{\mathrm{RV}}$ is estimated from three discrete points, as in (4), then the filter becomes

$$F_d(\alpha) = \frac{4}{3(\alpha R)^2}[1 - J_0(\sqrt{3}\alpha R)] \tag{10}$$

where J_0 is Bessel's function of the first kind of zero order. Figure 3 shows these two filters as a function of αR. For blue wavenumber spectra, aliasing might become significant. Our conclusions will turn out to be fairly insensitive to the exact structure of the filter at high wavenumbers. For analytical convenience we approximate both filters by a tophat filter

$$F(\alpha) = \begin{cases} 1 & \text{for } 0 < \alpha < \hat{\alpha} \\ 0 & \text{for } \hat{\alpha} < \alpha \end{cases} \tag{11}$$

of height one and cutoff wavenumber

$$\hat{\alpha} = \int_0^\infty d\alpha F_c(\alpha) \approx \int_0^\infty d\alpha F_d(\alpha) \approx \frac{1.7}{R} \tag{12}$$

also shown in Fig. 3.

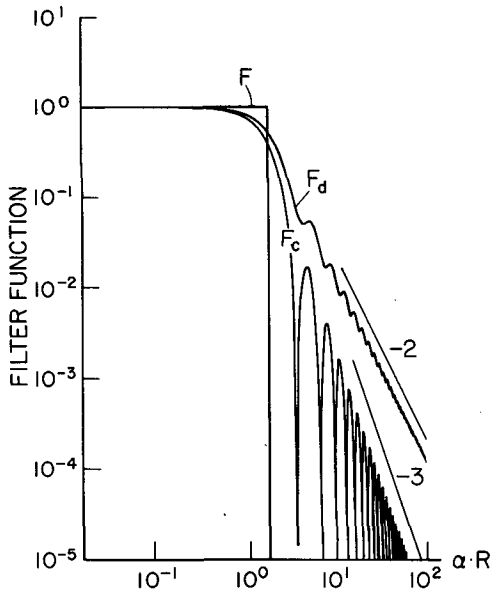

FIG. 3. Filters F_c, F_d and F as a function of normalized horizontal wavenumber αR. The filter F_c represents the effect of averaging over a circle, F_d the discrete estimate (4), and F the tophat approximation.

The cutoff wavenumbers $\hat{\alpha}_i$ for the different levels are listed in Table 1. To put these numbers in perspective, Fig. 4 shows a schematic view of horizontal and vertical wavenumber space. In vertical wavenumber space there exists a traditional classification (Munk, 1981): Gross-structure has vertical wavelengths larger than 10 m, finestructure wavelengths between 10 and 1 m, and microstructure wavelengths smaller than 1 m. This classification is motivated by the form of temperature gradient spectra which have changes of slope at 10 m and at 1 m (Gregg, 1977). Shear spectra (Gargett et al., 1981) are very similar to the temperature gradient spectra and also have changes of slope at 10 and 1 m. Although this classification is purely phenomenological, gross-structure is generally attributed to internal gravity waves, finestructure to stratified or buoyancy-modified turbulence and microstructure to intermittent 3-D turbulence. Indeed, Munk (1981) puts the internal wave cutoff at $\beta_c = 2\pi/10\ \text{m}^{-1} = 0.6\ \text{m}^{-1}$ in his 1981 version of the GM spectrum.

It seems that a similar classification may apply in horizontal wavenumber space. Dugan (1984) finds that his horizontal wavenumber spectra of temperature change slope at horizontal wavelengths of 250 and 25 m, with the field being very intermittent at wavelengths smaller than 25 m. This suggests that horizontal and vertical scales are related by an aspect ratio of the order of 1/25. In the microstructure range the aspect ratio is, of course, expected to rapidly approach one. If we follow this classification, the cutoff wavenumbers $\hat{\alpha}_i$ of the tophat filter fall into the microstructure range for level 2, into the finestructure range for level 5, and into the internal gravity wave range for level 6, 10 and 14. Only estimates at these latter levels represent variances from the internal gravity wave range, the estimates at the shallower depths include variance from the fine- and microstructure ranges. It will be shown that, even in the internal gravity wave range, not all of the observed variance is due to internal gravity waves.

5. Measurement errors

There are two types of measurement errors: systematic and random. Systematic errors are constant in time and affect only the mean value of the time series. They are most likely due to instrument offset errors. Estimation of such offset errors leads to the conclusion that the observed mean values represent instrument errors and not oceanic signals. The IWEX array is unable to resolve the mesoscale contribution to potential vorticity. (Note that the mean values of $\overline{VS}$ and $\overline{PV}$ are meaningless even in the absence of any systematic errors since the constant of integration in (5) is undetermined for each $\overline{VS}$ time series.)

Random instrument errors are fluctuating and affect variances and spectra. They usually show up as a white noise floor in the autospectra. No such noise floor is apparent in any of the spectra of $\overline{RV}$, $\overline{HD}$, $\overline{VS}$ and $\overline{PV}$ (Fig. 6). Instead, they all have a red frequency dependence with peaks or changes of slope at the Coriolis and Brunt–Väisälä frequency, which are oceanic and not instrumental parameters. Random noise does not seem to be a problem.

Part of the variance is due to incoherent current fluctuations that might represent instrumental noise

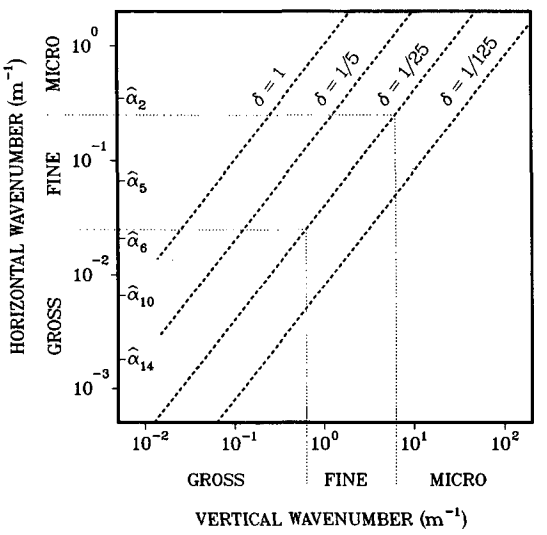

FIG. 4. Schematic partition of horizontal and vertical wavenumber space into gross-, fine- and microstructure. Lines of constant aspect ratio $\delta = \alpha/\beta$ are indicated. Also shown are the cutoff wavenumbers $\hat{\alpha}_i$ of the tophat filter (11) for level 2 to 14.

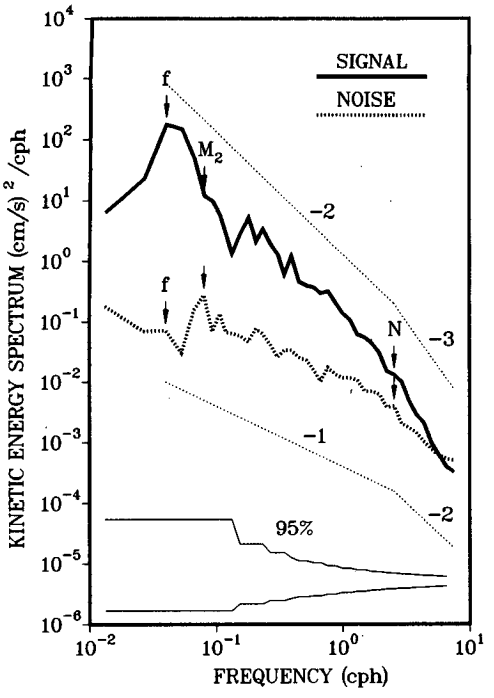

FIG. 5. Partition of the averaged kinetic energy spectrum at level 2 into "signal" and "noise". The "signal" represents the current fluctuations which are coherent among the three current meters. The "noise" represents the current fluctuations which are incoherent.

and not oceanic currents with horizontal scales smaller than the smallest current meter separation (8.5 m at level 2). This incoherent component can be determined by decomposing each of the three velocity time series at level 2 into a "signal" and "noise" contribution

$$\left.\begin{aligned} u_k &= \hat{u}_k + \delta u_k \\ u_k &= \hat{v}_k + \delta v_k \end{aligned}\right\}, \quad k = A, B, C \tag{13}$$

and assuming that the signal contributions are totally coherent whereas the noise contributions are totally incoherent. The autospectra and coherences squared are then given by

$$\langle u_k u_k^* \rangle = \langle \hat{u}_k \hat{u}_k^* \rangle + \langle \delta u_k \delta u_k^* \rangle,$$

$$\frac{\langle u_k u_{k'}^* \rangle \langle u_k^* u_{k'} \rangle}{\langle u_k u_k^* \rangle \langle u_{k'} u_{k'}^* \rangle} = \frac{\langle \hat{u}_k^* \hat{u}_k \rangle \langle \hat{u}_k^* \hat{u}_{k'} \rangle}{(\langle \hat{u}_k \hat{u}_k^* \rangle + \langle \delta u_k \delta u_k^* \rangle)(\langle \hat{u}_{k'} \hat{u}_{k'}^* \rangle + \langle \delta u_{k'} \delta u_{k'}^* \rangle)} \tag{14}$$

with corresponding formulas for the meridional velocity component v. These twelve relationships allow determination of six signal autospectra and six noise autospectra from the observed six autospectra and the observed six co- and quad-spectra. The average of all six signal autospectra, $\hat{S}_u(\omega)$, and the average of all six noise spectra, $\delta S_u(\omega)$, are shown in Fig. 5. The signal spectrum contains most of the variance and has a -2 slope in the f to N band and a -3 slope in the band beyond N. The noise spectrum $\delta S_u(\omega)$ represents the "current noise" in the terminology of Müller et al. (1978). It has a -1 slope in the f to N band and a -2 slope in the band beyond N. The rms value is $\delta u = 2.3 \times 10^{-3}$ m s^{-1}. Its contribution to the spectra of $\overline{\mathrm{RV}}$ and $\overline{\mathrm{HD}}$ is given by

$$\delta S_{\overline{\mathrm{RV}}}(\omega) = \delta S_{\overline{\mathrm{HD}}}(\omega) = a^2 \frac{4}{9R^2} \delta S_u(\omega) \tag{15}$$

and to the $\overline{\mathrm{VS}}$ and $\overline{\mathrm{PV}}$ spectra by

$$S_{\overline{\mathrm{VS}}}(\omega) = a^2 \frac{4}{9R^2} \frac{f^2}{\omega^2} \delta S_u(\omega)$$

$$\delta S_{\overline{\mathrm{PV}}}(\omega) = a^2 \frac{4}{9R^2} [\delta S_{\overline{\mathrm{RV}}}(\omega) + \delta S_{\overline{\mathrm{VS}}}(\omega)] \tag{16}$$

with $a = \sqrt{3}$. To be on the safe side one might want to subtract these contributions from the observed spectra. We will not do so but will point out the implied uncertainties in our estimates.

6. Variances

The variances of the time series $\overline{\mathrm{RV}}(t)$, $\overline{\mathrm{HD}}(t)$, $\overline{\mathrm{VS}}(t)$ and $\overline{\mathrm{PV}}(t)$ are listed in Table 2, together with the rms values normalized by f and the noise variances. The variance of $\overline{\mathrm{RV}}$ represents the enstrophy of the fluid motion. The normalized rms values of $\overline{\mathrm{RV}}$ and $\overline{\mathrm{HD}}$ are estimates of the Rossby number, U/fL, the normalized value of $\overline{\mathrm{VS}}$ is the rms vertical strain. There are some huge numbers in the table. At level 2, the normalized rms values are of the order of 10, implying Rossby numbers O(10) and vertical strain values O(10).

These values are, however, not inconsistent with what little other information there exists. Values of the vertical strain can also be obtained by vertically differencing isopycnal displacements. Using CTD data from off the California coast Pinkel et al. (1987) find rms vertical strain values of 0.17, 0.26 and 0.38 for vertical differencing intervals of 20 m, 10 m and 5 m, respectively. These values are consistent with our values of 0.13, 0.34 and 0.85 obtained from horizontal differencing intervals of 925 m, 260 m and 80.3 m (Table 1) if one assumes, as in Fig. 4, an aspect ratio of about 1/25. At level 2, up to 60% of the variance is due to current noise, at level 14 less than 10%, so subtraction of current noise will not affect the qualitative results.

7. Frequency spectra

Frequency spectra of all time series are displayed in Fig. 6. All the spectra are red and decrease in amplitude from level 2 to level 14. The spectra of $\overline{\mathrm{RV}}$ and $\overline{\mathrm{HD}}$ exhibit a peak at f and a change of slope from approximately $-3/2$ to -2 at N. The spectrum of $\overline{\mathrm{VS}}$ can be obtained by multiplying the spectrum of $\overline{\mathrm{HD}}$ by f^2/ω^2 or more correctly by $f^2(\Delta t)^2/(2 - 2\cos\omega\Delta t)$ if one takes

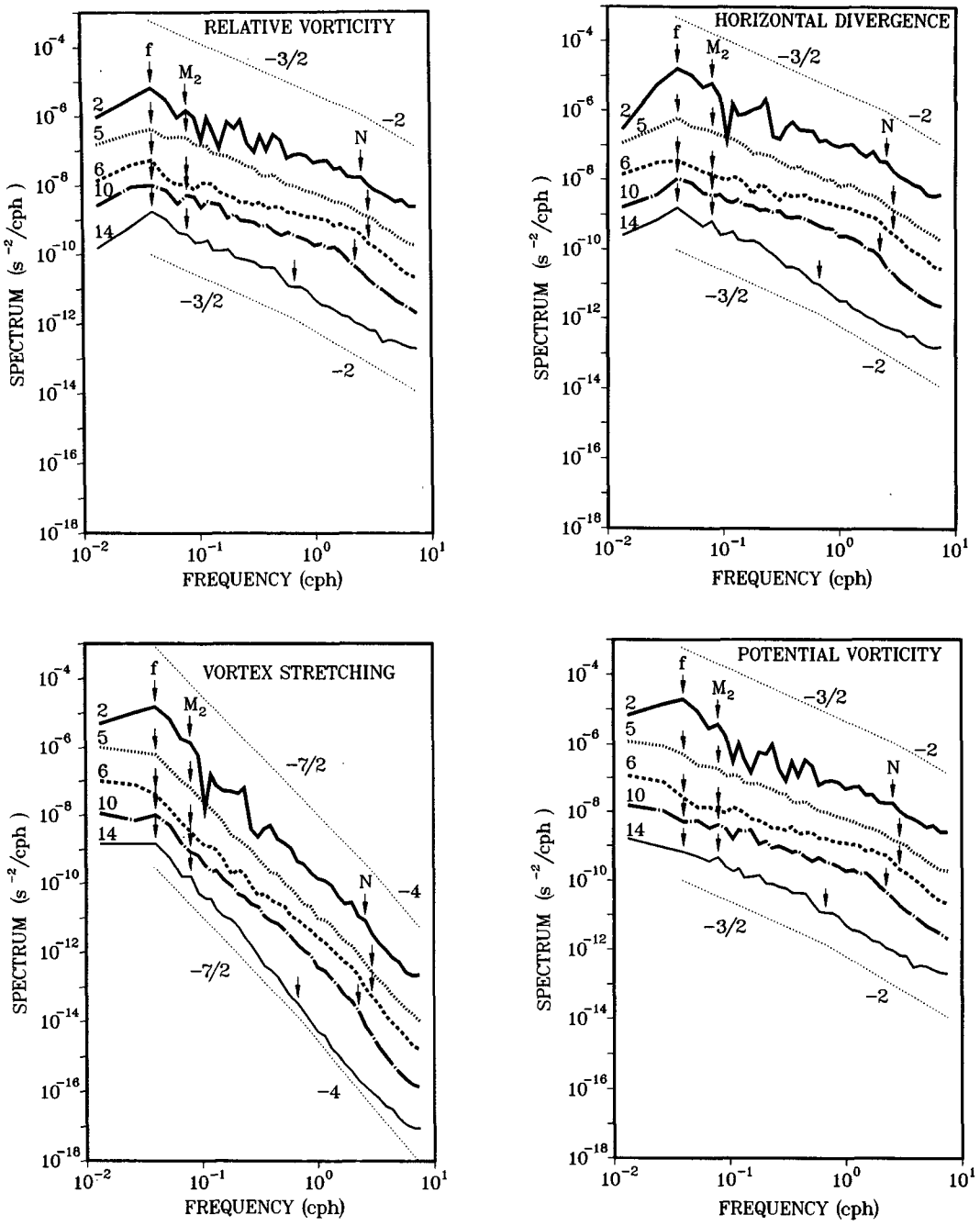

FIG. 6. Frequency spectra of area averaged relative vorticity, horizontal divergence, vortex stretching and potential vorticity at IWEX levels 2, 5, 6, 10 and 14.

the discrete sampling interval Δt into account. The spectrum of $\overline{VS}$ therefore shows a suppressed (or no) peak at f and steeper slopes. The potential vorticity spectra show no peak at f and $-3/2$ and -2 slopes. The spectra at level 2 show the largest scatter because they are derived from the shortest time series (Table 1). The spectra are very different from kinetic energy spectra which have a strong peak at f, a -2 slope in the f to N band, and a -3 slope beyond N.

Potential vorticity is the sum of relative vorticity RV and vortex stretching VS. For internal gravity waves RV = $-$VS and the potential vorticity vanishes. If the fluctuations were internal gravity waves the observed spectra of $\overline{RV}$ and $\overline{VS}$ should be equal. This is clearly not the case in Fig. 7. Vortex stretching dominates at low frequencies, relative vorticity at high frequencies. Figure 7 also shows the Garrett and Munk internal wave model prediction (See appendix B for

TABLE 2. Total variance, root-mean-square value divided by f, and noise variance of the time series $\overline{RV}$, $\overline{HD}$, $\overline{VS}$, and $\overline{PV}$ at the five levels 2, 5, 6, 10 and 14. The noise variance is defined as that part of the variance which is caused by incoherent current fluctuations.

	Level	Radius [m]	$\overline{RV}$	$\overline{HD}$	$\overline{VS}$	$\overline{PV}$
Total variance [s^{-2}]			4.5×10^{-7}	1.1×10^{-6}	5.6×10^{-7}	9.9×10^{-7}
rms/f	2	4.9	9.9	15	11	15
Noise variance [s^{-2}]			2.8×10^{-7}	2.8×10^{-7}	1.4×10^{-7}	4.3×10^{-7}
Total variance [s^{-2}]			5.2×10^{-8}	6.2×10^{-8}	3.8×10^{-8}	7.0×10^{-8}
rms/f	5	25.4	3.4	3.7	2.9	4.0
Noise variance [s^{-2}]			1.1×10^{-8}	1.1×10^{-8}	5.3×10^{-9}	1.6×10^{-8}
Total variance [s^{-2}]			5.8×10^{-9}	7.0×10^{-9}	3.3×10^{-9}	7.2×10^{-9}
rms/f	6	80.3	1.1	1.3	0.85	1.3
Noise variance [s^{-2}]			1.1×10^{-9}	1.1×10^{-9}	5.3×10^{-10}	1.6×10^{-9}
Total variance [s^{-2}]			1.3×10^{-9}	1.4×10^{-9}	5.1×10^{-10}	1.4×10^{-9}
rms/f	10	260	0.54	0.56	0.34	0.54
Noise variance [s^{-2}]			1.0×10^{-10}	1.0×10^{-10}	5.1×10^{-11}	1.5×10^{-10}
Total variance [s^{-2}]			1.1×10^{-10}	1.1×10^{-10}	7.4×10^{-11}	7.4×10^{-11}
rms/f	14	925	0.15	0.15	0.13	0.13
Noise variance [s^{-2}]			7.9×10^{-12}	7.9×100^{-12}	4.0×10^{-12}	1.2×10^{-11}

details). At level 14, 10 and 6 it represents reasonably well the $\overline{VS}$ spectrum in the f to N band, but falls short at levels 5 and 2. The same is true for the $\overline{HD}$ spectra. This might be taken as an indication that the observed VS and HD fields reflect internal gravity waves. The predictions at levels 2 and 5 fall short simply because the Garrett and Munk model has a vertical cutoff wavenumber $\beta_c = 2\pi/10$ m^{-1} and does not represent motions at smaller scales whereas we argued in Fig. 4 that levels 2 and 5 include variances from fine- and microstructure scales. The supposition can, however, not be proven with our measurements of $\overline{RV}$ and $\overline{VS}$. A rigorous decomposition into internal gravity and vortical motions requires additional measurements.

8. Horizontal scales

For each variable, the level of the spectrum decreases monotonically from level 2 to level 14. (The one point where the level 2 $\overline{HD}$ and $\overline{VS}$ spectrum is smaller than the level 5 spectrum is presumably due to the large uncertainty of level 2 spectra.) This monotonic decrease can be attributed either to the fact that spectra taken at different depths are in a different physical environment or to the fact that we average over a larger and larger area with increasing depth. Since levels 2 to 10 all lie in the main thermocline where N varies little, changes in the spectral level are likely to reflect changes in averaging area rather than changes in physical environment. This might even be true for level 14 where N is about one quarter of the main thermocline value (Table 1). Internal gravity wave WKB scaling predicts $\xi \sim N^{-1}$ and $\beta \sim N$ and hence $\overline{VS} = -f\partial_3\xi$ to be depth independent. In contrast, Fig. 6 displays a one order of magnitude decrease in spectral amplitude from level 10 to level 14. Indeed, the Garrett and Munk estimates for levels 10 and 14 would be identical were it not for the different averaging areas. Therefore, we assume a homogeneous physical environment and ascribe differences between the spectra at different levels to different averaging areas so that the difference between successive spectra gives information about the distribution of variance with horizontal wavenumber. Formally, the difference between two successive spectral estimates at level i and $i + 1$ is given by

$$S_i(\omega) - S_{i+1}(\omega) = \int_0^\infty d\alpha\, [F^i(\alpha) - F^{i+1}(\alpha)]S(\alpha, \omega) = \int_{\hat{\alpha}_{i+1}}^{\hat{\alpha}_i} d\alpha S(\alpha, \omega) \tag{17}$$

where $S(\alpha, \omega)$ is the horizontal wavenumber–frequency spectrum and $F^i(\alpha)$ the tophat filter (11) at level i. The quantity

$$\hat{S}(\alpha_i, \omega) = \frac{S_i(\omega) - S_{i+1}(\omega)}{\hat{\alpha}_i - \hat{\alpha}_{i+1}} \tag{18}$$

is hence an estimate of the wavenumber–frequency spectrum at wavenumber $\alpha_i = (\hat{\alpha}_i + \hat{\alpha}_{i+1})/2$. Perspective plots of these spectra are shown in Fig. 8. Here, and in the following, estimates are presented at all five wavenumbers: α_{14}, α_{10}, α_6, α_5 and α_2. The estimates at α_{14} are the least reliable because they depend solely on measurements at level 14 for which our homogeneity assumption is least applicable. We present α_{14}-estimates, but do not rely on them for inferences.

In Fig. 8, the wavenumber dependence is similar for all frequencies, so it is sufficient to discuss the wavenumber spectra

$$\hat{S}(\alpha_i) = \int d\omega \hat{S}(\alpha_i, \omega) \tag{19}$$

which are obtained by integrating over all frequencies.

These wavenumber spectra are displayed in Fig. 9 and have slopes of about +2/3. Most of the variance is at the smallest scales. The slope is diminished somewhat if one subtracts that part of the signal which is due to current noise. The blue behavior might raise concern about our tophat filter approach. However, use of the exact filter (9) would only shift the spectrum. The observed variance difference would not be ascribed to the wavenumber $\alpha_i = (\hat{\alpha}_i + \hat{\alpha}_{i+1})/2$ but to a larger wavenumber.

9. Vertical scales

Vertical scales are usually inferred from the coherences between time series at different depths. The IWEX array is completely incoherent with respect to $\overline{RV}$, $\overline{HD}$, $\overline{VS}$ and $\overline{PV}$. All vertical coherences do not differ significantly from zero. However, this result does not put any precise bounds on the vertical coherence scale or vertical wavenumber bandwidth since the time series at different depths represent averages over different horizontal areas and degradation of coherence is caused by both vertical and horizontal destructive interference. Information about vertical scales is, however, obtained by interpreting the observed frequencies as Doppler-shifted frequencies.

The potential vorticity field represents, by definition, the vortical mode. Its dynamics at small scales is not known. In the linear limit the vortical mode represents steady horizontal flows. The observed time dependence of potential vorticity would be due to advection then, either nonlinear self-advection or by internal gravity waves. Indeed, the observed slopes of the potential vorticity spectra, $-3/2$ in the f to N band and -2 in the band beyond N (Fig. 6), are suggestive of the "finestructure contamination" model of McKean (1974). This model assumes that a steady layered structure is vertically advected past a fixed sensor by internal gravity waves. The model was originally formulated to address temperature finestructure contamination but can be applied to any scalar field. Following McKean we must make the following statistical assumptions:

- The advected steady potential vorticity profile PV(z) consists of random layers with random increments ΔPV from layer to layer.
- The increments have a Gaussian distribution with zero mean and variance $\langle(\Delta\text{PV})^2\rangle$.
- The number of layers per unit depth follows a Poisson distribution characterized by a mean layer thickness h.
- The advecting internal wave field is a Gaussian process.
- The vertical displacement field has a band-limited spectrum $P(\omega) \sim \omega^{-2}$ for $f < \omega < N$ of variance $\langle\xi^2\rangle$.

Then, McKean's theory predicts that the frequency spectrum at a moored sensor is given by

$$S(\omega) = \frac{\langle(\Delta\text{PV})^2\rangle}{h} \times \langle\xi^2\rangle^{1/2} \frac{1}{f} \begin{cases} \frac{1}{\sqrt{2}}(\omega/f)^{-3/2} & \text{for } f < \omega < N \\ \frac{2}{\pi}(N/f)^{1/2}(\omega/f)^{-2} & \text{for } N < \omega \end{cases} \tag{20}$$

with slopes $-3/2$ and -2, as observed, and variance

$$V = \sqrt{2}\,\frac{\langle(\Delta\text{PV})^2\rangle}{h}\,\langle\xi^2\rangle^{1/2}. \tag{21}$$

If we accept this model, we can infer the parameter combination

$$d = \frac{\langle(\Delta\text{PV})^2\rangle}{h} \tag{22}$$

from the level or variance of the observed potential vorticity spectra since the rms vertical displacement $\langle\xi^2\rangle^{1/2}$ in (20) or (21) can independently be estimated from the temperature measurements in IWEX. These displacement estimates have their own finestructure contamination problem. The WKB scaled rms displacements listed in Table 1 represent decontaminated estimates reflecting more accurately the actual internal wave displacements (Müller et al., 1978).

The parameter d also determines the level of the vertical wavenumber spectrum of PV(z) which is given by

$$S(\beta) = \frac{2d}{\beta^2} \tag{23}$$

and has infinite variance. That part of the variance that is advected to supra-inertial frequencies and represented in (20) comes primarily from large vertical wavenumbers. If we assume that it comes from wavenumbers larger than a cutoff wavenumber β_*, then the variance (21) must be equal to

$$V = \int_{\beta_*}^{\infty} d\beta S(\beta) = \int_{\beta_*}^{\infty} d\beta 2d\beta^{-2} = 2d\beta_*^{-1}. \tag{24}$$

Comparison of (21) and (24) yields an estimate of the cutoff wavenumber

$$\beta_* = \sqrt{2}/\langle\xi^2\rangle^{1/2}. \tag{25}$$

In McKean's model, most of the variance seen at supra-inertial frequencies originates from vertical scales comparable to the rms vertical displacement of the advecting internal wave field. If we repeat this argument for each of the five horizontal wavenumber bands separately, we find the variance in the band between $\hat{\alpha}_{i+1}$ and $\hat{\alpha}_i$

$$V_i = \frac{2(d_i - d_{i+1})}{\beta_*^i} = \sqrt{2}\,(d_i\langle\xi_i^2\rangle^{1/2} - d_{i+1}\langle\xi_{i+1}^2\rangle^{1/2}) \tag{26}$$

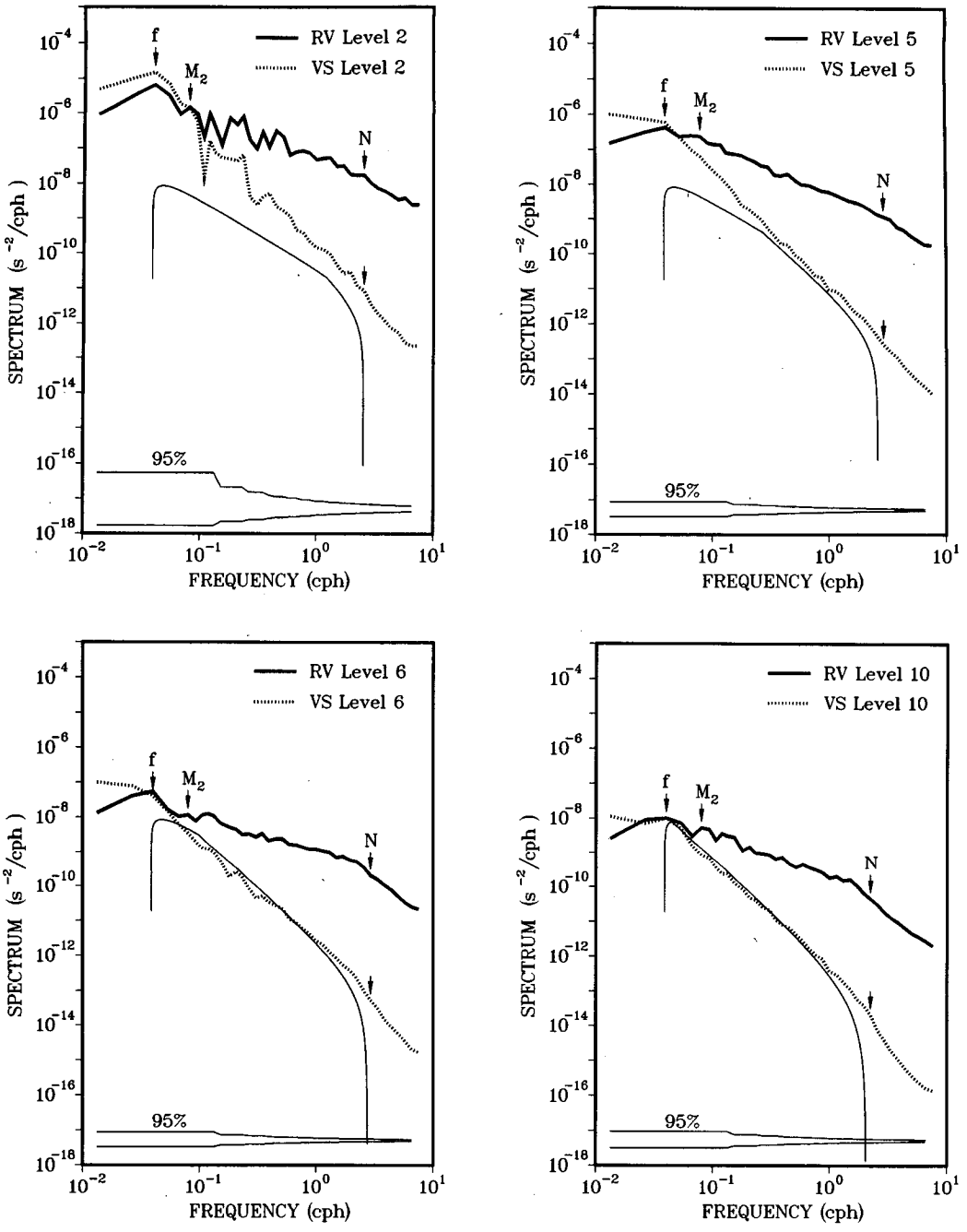

FIG. 7. Frequency spectra of relative vorticity and vortex stretching at IWEX levels 2, 5, 6, 10 and 14. The smooth line is the prediction of the GM 76 spectrum. (See appendix B for details).

and hence

$$\beta^i_* = \sqrt{2}\left[\frac{d_i}{d_i - d_{i+1}}\langle\xi_i^2\rangle^{1/2} - \frac{d_{i+1}}{d_i - d_{i+1}}\langle\xi_{i+1}^2\rangle^{1/2}\right]^{-1} \tag{27}$$

for the cutoff wavenumber centered at $\alpha_i = (\hat{\alpha}_i + \hat{\alpha}_{i+1})/2$. This cutoff wavenumber is about 0.2 m^{-1}, except at the lowest wavenumber band (Fig. 10) and implies an aspect ratio $\delta = \alpha/\beta$ which decreases from about 1 in the highest wavenumber band to about 1/60 in the lowest wavenumber band.

McKean's theory ascribes all of the high frequency variance to vertical advection, neglecting horizontal advection. This is permissible as long as the aspect ratio of the advected field is less than w/u, where w is the

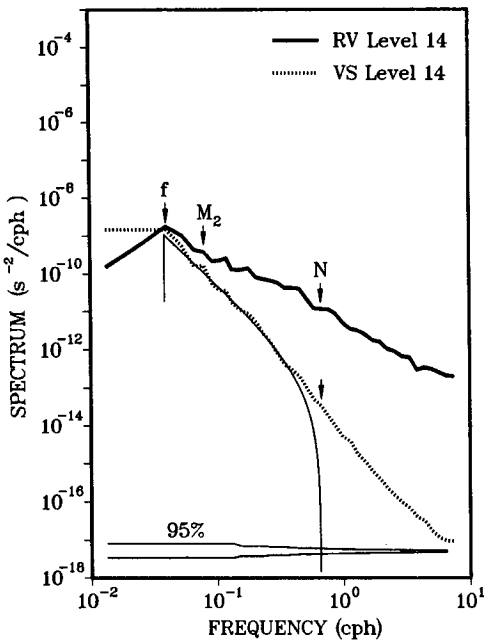

FIG. 7. (*Continued*)

vertical and u the horizontal advection velocity. Since typical Garrett and Munk estimates are $w \approx$ O(0.5 cm s^{-1}) and $u \approx$ O(5 cm s^{-1}) aspect ratios less than O(0.1) are required, inconsistent with our estimates at high horizontal wavenumbers. The cutoff wavenumbers β_* in Fig. 10 must hence be regarded as upper limits. They are required if all variance is due to vertical advection but they can be smaller if part of the variance is due to horizontal advection.

10. Model spectrum

The observed amplitudes and scales of the small-scale potential vorticity field can be summarized by a model wavenumber–frequency spectrum of the separable form

$$S_{PV}(\alpha, \beta, \omega) = VA(\alpha)B(\beta)C(\omega) \qquad (28)$$

where V is the total variance; $A(\alpha)$ the normalized horizontal wavenumber spectrum; $B(\beta)$ the normalized vertical wavenumber spectrum; and $C(\omega)$ the normalized intrinsic frequency spectrum. In the resolved horizontal wavenumber range from $\alpha_{min} = \alpha_{10} \approx 4.3 \times 10^{-3}$ m^{-1} to $\alpha_{max} = \alpha_2 \approx 0.2$ m^{-1}, $A(\alpha)$ can be approximated by a power law

$$A(\alpha) = \frac{n+1}{\alpha_{max}}\left[\frac{\alpha}{\alpha_{max}}\right]^n, \quad \alpha_{min} < \alpha < \alpha_{max} \qquad (29)$$

with $n \approx 2/3$ (see Fig. 9). Here we have chosen α_{10} as the lowest resolved wavenumber because estimates at α_{14} might include the effect of inhomogeneities in the physical environment. The vertical wavenumber dependence is also characterized by a power law

$$B(\beta) = \frac{\beta_*}{\beta^2} \quad \text{for} \quad \beta_* < \beta \qquad (30)$$

with $\beta_* = 0.2$ m^{-1} independent of α (see Fig. 10). The β^{-2} behavior is solely a consequence of McKean's statistical assumptions about the advected potential vorticity field (random layering, Poisson statistics for layer thicknesses, Gaussian statistics for increments). The wavenumber scale β_* was obtained by matching the predicted to the observed variance. The frequency spectrum is approximated by $C(\omega) = \delta(\omega)$ since we regard the intrinsic frequency of the potential vorticity field as small or zero. The high observed frequencies are the product of Doppler shifting. For the variance we estimated a value $V = 10^{-6}$ s^{-2} (Table 2) in the resolved wavenumber–frequency range. Since the horizontal wavenumber spectrum $A(\alpha)$ is blue, the value is primarily due to contributions from near the high wavenumber cutoff α_{max} and might be underestimated.

Theory uniquely relates the amplitudes of the velocity and displacement field of the vortical mode to the amplitude of the potential vorticity field (see the amplitude relations A6 and A8 in appendix A). The model spectrum (28) hence implies model spectra for the total (kinetic plus available potential) energy of the vortical mode

$$S_E(\alpha, \beta, \omega) = \frac{1}{2}\left[\alpha^2 + \frac{f^2}{N^2}\beta^2\right]^{-1} S_{PV}(\alpha, \beta, \omega) \qquad (31)$$

and for the inverse Richardson number

$$S_{R_i^{-1}}(\alpha, \beta, \omega) = \frac{\alpha^2\beta^2}{N^2}\left[\alpha^2 + \frac{f^2}{N^2}\beta^2\right]^{-2} S_{PV}(\alpha, \beta, \omega). \qquad (32)$$

Projections of these model spectra onto horizontal wavenumbers are shown in Fig. 11. These horizontal wavenumber spectra represent the energy and (normalized) vertical shear due to vortical motions. Figure 11 also shows the total energy and inverse Richardson number spectra of the internal gravity mode, as calculated from the Garrett and Munk model spectrum (for algebraic details see appendix B). The variances of these spectra are listed in Table 3. They are obtained by integrating the vortical mode spectra from α_{10} to α_2 and the internal gravity wave spectra from zero to infinity. Figure 11 shows that the vortical mode dominates the gravity mode in the resolved wavenumber band α_{10} to α_2. Furthermore, the numbers in Table 3 demonstrate that small-scale vortical motions in the band α_{10} to α_2 contribute little to the overall energy (only 10% for our model calculations) but represent the major fraction of the overall shear (about 60% for our model calculations).

Comparison with the Garrett and Munk spectrum may not accurately reflect the actual vortical and gravity component of the oceanic shear. The Garrett and

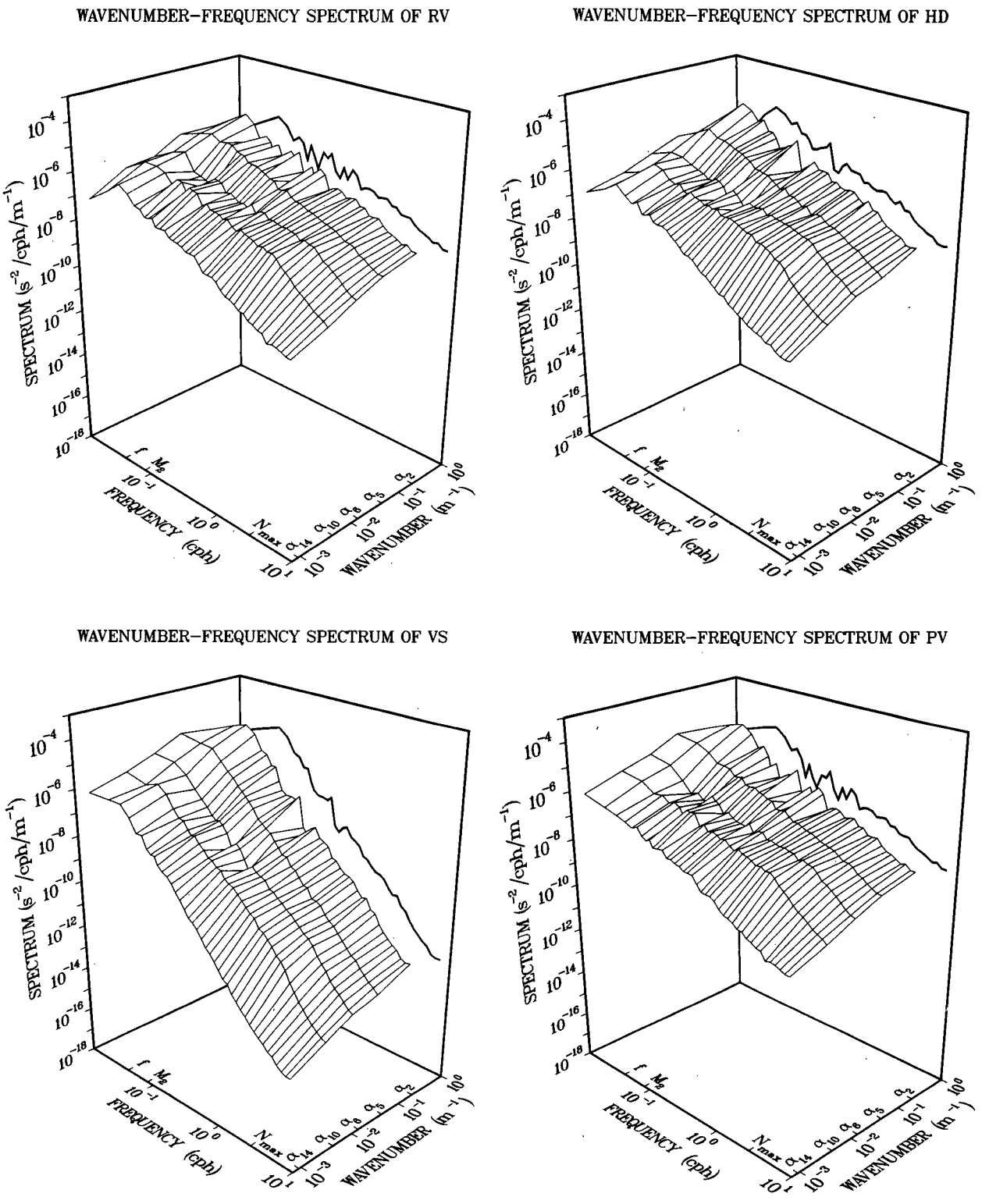

FIG. 8. Perspective plot of the horizontal wavenumber–frequency spectrum of relative vorticity, horizontal divergence, vortex stretching, and potential vorticity. The curves on the ordinate plane are the frequency spectra, obtained by integrating over horizontal wavenumber, and are identical to the frequency spectra at level 2. The one point in the level 2 horizontal divergence and vortex stretching spectrum smaller than the level 5 spectrum was replaced by an interpolated value.

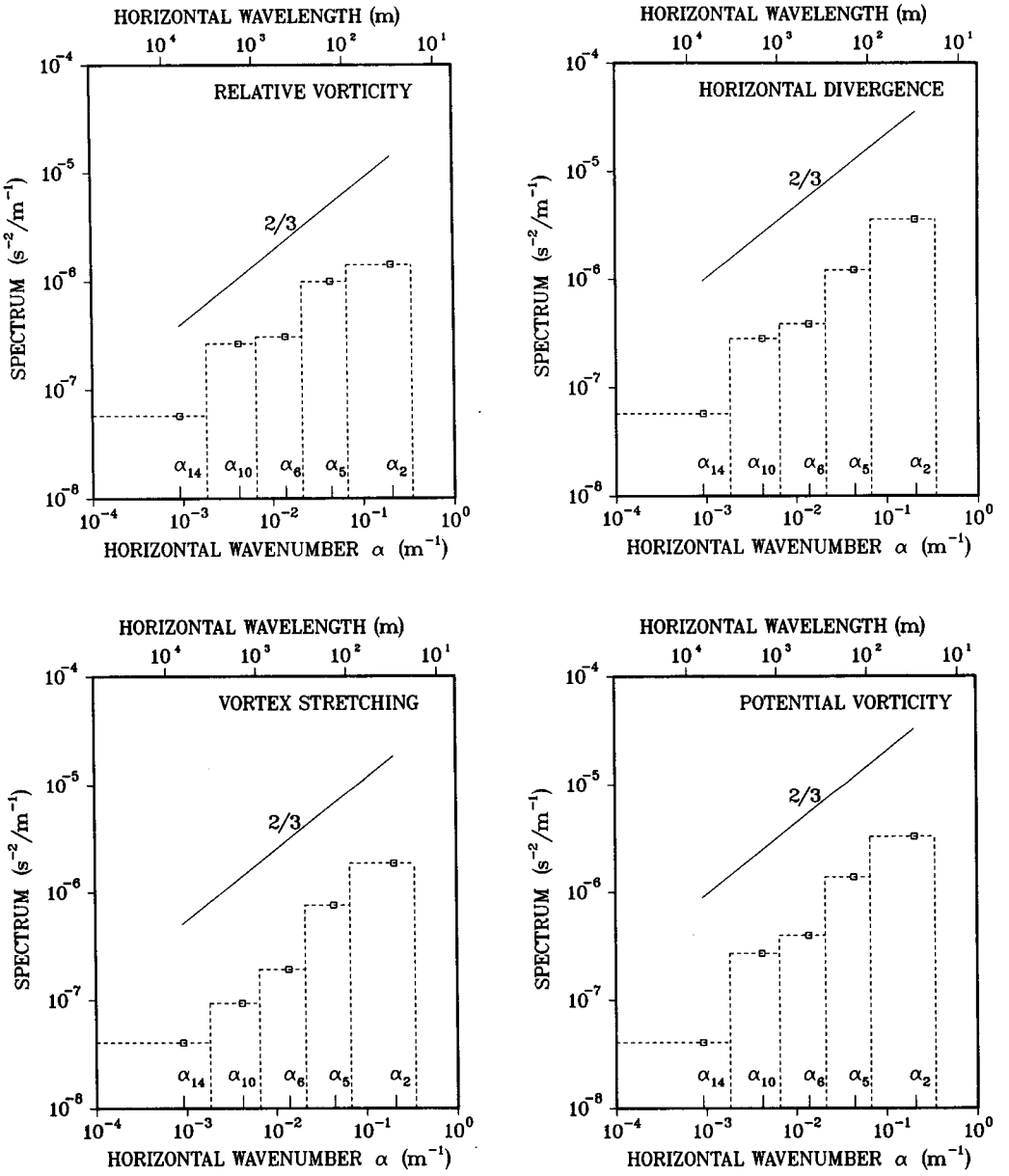

FIG. 9. Horizontal wavenumber spectrum of relative vorticity, horizontal divergence, vortex stretching and potential vorticity. Estimates are obtained at the five wavenumbers $\alpha_i = (\hat{\alpha}_i + \hat{\alpha}_{i+1})/2$. The best fit slope to the four high wavenumber points is approximately +2/3.

Munk spectrum is based on data that do not adequately sample the high-wavenumber, high-frequency part and may hence not accurately describe the internal wave shear. A direct normal mode decomposition of the shear is needed.

11. Summary and discussion

The principal findings of this paper are the variance, and the space- and time-scales of the small-scale potential vorticity field. "Potential vorticity" refers to the quantity $PV = f + (\partial_x v - \partial_y u) - f\partial_z \xi$ which is the sum of planetary vorticity, relative vorticity and vortex stretching and represents a linear version of Ertel's (1942) potential vorticity. The quantity PV defines the vortical mode in a normal mode decomposition. Determining the amplitude, and the space- and time-scales of PV is therefore equivalent to determining those of the vortical mode. The estimates of PV are obtained from the IWEX mooring, making use of its unique trimoored design. The specific results are:

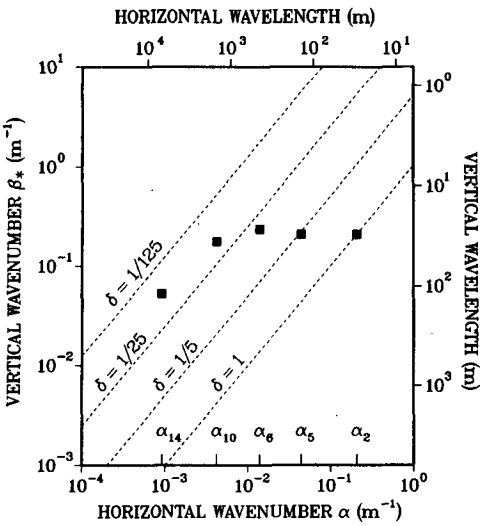

FIG. 10. Estimates of the vertical cutoff wavenumber β_* for the five different horizontal wavenumber bins centered at $\alpha_i = (\hat{\alpha}_i + \hat{\alpha}_{i+1})/2$. The lines of constant aspect ratio $\delta = \alpha/\beta$ indicate that the aspect ratio decreases from about one at α_2 to about 1/60 at α_{14}.

- The variance or enstrophy of the small-scale potential vorticity field is about 10^{-6} s^{-2}.
- Time series of PV show a broad range of time scales. Frequency spectra have no pronounced peak at f, a $-3/2$ slope in the f to N band, and a -2 slope in the band beyond N.
- The horizontal wavenumber spectrum is blue with a slope of approximately $+2/3$, so most of the variance is at the smallest horizontal scales. The resolved horizontal scales range from about 5 m to about 260 m (or to about 1 km if one includes level 14).
- The observed frequencies are interpreted as apparent frequencies caused by Doppler shifting. A low frequency, steppy potential vorticity profile is vertically advected past the current meter array by internal gravity waves.
- The advected potential vorticity field is characterized by a vertical scale β_*^{-1} which is of the order of 5 m, independent of horizontal wavenumber. This scale implies an aspect ratio decreasing from about 1 at small horizontal scales to about 1/60 at large horizontal scales.

All these results are summarized in a model wavenumber–frequency spectrum. It is the first time that these quantities are estimated. The major assumptions that went into the analysis were:

- In estimating vortex stretching, the linear relation $\partial_t \xi = w$ was used, instead of the exact relation $D\xi/Dt = w$. This is acceptable as long as the horizontal and vertical strains are smaller than one.
- In estimating the horizontal wavenumber spectrum, a homogeneous environment was assumed. The differences in spectra at successive levels were solely ascribed to differences in the averaging area.
- In applying McKean's theory, horizontal Doppler shifting was neglected. This is acceptable as long as the advected potential vorticity field has sufficiently small aspect ratios.

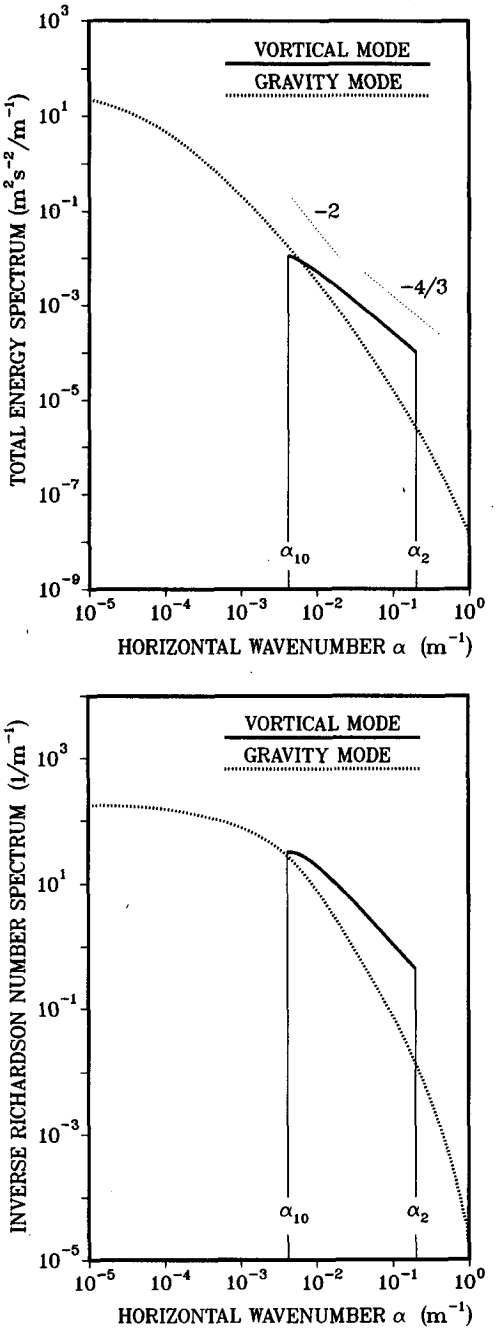

FIG. 11. Model horizontal wavenumber spectra of total energy and inverse Richardson number for the vortical and gravity mode. The vortical mode spectra are calculated using the model spectrum (28) with $B(\beta) = \delta(\beta - \beta_*)$ and $\beta_* = 0.2$ m^{-1} and are limited to the wavenumber band α_{10} to α_2. The internal gravity wave spectra are calculated using the GM 76 spectrum as defined in appendix B. The variances of the spectra are listed in Table 3.

TABLE 3. Model total energy and inverse Richardson number for the vortical and gravity mode. The numbers are obtained by integrating the vortical mode spectra in Fig. 11 from α_{10} to α_2 and the internal wave spectra from zero to infinity.

	Vortical mode	Gravity mode
Total energy ($m^2 s^{-2}$)	2.0×10^{-4}	2.2×10^{-3}
Inverse Richardson number	0.71	0.42

These assumptions cannot be justified rigorously and the limitation they might impose need to be considered. Indeed, some of our results are inconsistent with these assumptions and forced us to weaken some of our statements, e.g., the vertical scale β_*^{-1} had to be interpreted as the smallest possible scale.

The most obvious extensions of our analysis would be to

- perform a complete normal mode decomposition into vortical and internal gravity modes, and
- estimate Ertel's potential vorticity.

A complete normal mode decomposition requires the incorporation of temperature data and a much more complex analysis which also considers the temperature finestructure contamination problem. Using theory, we estimated the energy and shear in the vortical mode and compared it to Garrett and Munk's estimates of the energy and shear in the internal gravity mode. The vortical mode dominates the total energy and shear spectrum in the resolved horizontal scale range from 5 to 260 m. This comparison with the Garrett and Munk spectrum might not be entirely fair since the Garrett and Munk spectrum may not accurately reflect internal wave levels at high wavenumbers and frequencies. However, the observed inverse Richardson number of the vortical mode of about 0.7 indicates that small-scale vortical motions contain a major fraction of the oceanic shear.

Ertel's potential vorticity is a nonlinear quantity and cannot be used in any decomposition of the flow field. Any such decomposition is an intrinsically linear operation requiring the validity of the superposition principle. Ertel's potential vorticity is, however, an important dynamical quantity since it is an invariant or conservative tracer for inviscid and adiabatic flows. Its measurement would be extremely useful. We estimated its linear parts, namely PV, but are unable to estimate the isopycnal tilt terms (which are presumably the largest nonlinear contribution, F. Henyey, personal communication) in any straightforward manner from the IWEX array.

Despite these problems and limitations this is the first time that some basic characteristics of the small-scale potential vorticity field are estimated. These estimates will hopefully help to disentangle the kinematics and dynamics of small-scale motions and their role in transferring energy and enstrophy from the large generation to the small dissipation scales.

Acknowledgments. The authors would like to thank M. Briscoe for his help with the IWEX data, G. Holloway, F. Henyey and R. Pinkel for many fruitful discussions and especially E. Kunze whose detailed comments on an earlier version greatly helped to improve the paper. K. Chong Morgan, J. Furuta and L. Takimoto provided expert technical assistance. This work was supported by the Office of Naval Research and is Contribution No. 1977 from the Hawaii Institute of Geophysics.

APPENDIX A

Normal Mode Decomposition

The linear equations of motion for an incompressible Boussinesq fluid are

$$\partial_t \mathbf{u} = -\xi N^2 \hat{\mathbf{z}} - f\hat{\mathbf{z}} \times \mathbf{u} - \nabla p \tag{A1a}$$

$$\partial_t \xi = \mathbf{u} \cdot \hat{\mathbf{z}} \tag{A1b}$$

$$\nabla \cdot \mathbf{u} = 0. \tag{A1c}$$

Here $\mathbf{u} = (u, v, w)$ is the velocity vector, ξ the vertical displacement, $\hat{\mathbf{z}}$ the vertical unit vector, p the excess pressure above hydrostatic divided by density, f the Coriolis frequency, $N^2 = -g\rho_0^{-1}\partial\tilde{\rho}/\partial z$ the square of the Brunt–Väisälä frequency, and $\tilde{\rho}(z)$ the background density. The equations (A1) assume f-plane dynamics and absence of dissipation and forcing. Only the variables u, v, and ξ are prognostic. The vertical velocity can be determined diagnostically from the incompressibility condition (A1c). The pressure is obtained from $\partial_t(\nabla \cdot \mathbf{u}) = 0$ which implies

$$\nabla^2 p = -\partial_z(\xi N^2) + f\hat{\mathbf{z}} \cdot (\nabla \times \mathbf{u}) \tag{A2}$$

and replaces the vertical momentum balance. The excess density $\delta\rho$ can be determined from

$$\delta\rho(\mathbf{x}, t) = \tilde{\rho}[z - \xi(\mathbf{x}, t)] - \tilde{\rho}(z) \tag{A3}$$

which reduces to

$$\delta\rho = -\xi \frac{\partial \tilde{\rho}}{\partial z} \tag{A4}$$

in the linear limit.

Assume an unbounded ocean and a constant Brunt-Väisälä frequency and solutions where each variable depends on space and time through the factor $\exp[i(\mathbf{k} \cdot \mathbf{x} - \omega t)]$, where $\mathbf{k} = (k_x, k_y, k_z)$ is the wave vector and ω the (Eulerian) frequency. The equations of motion are then converted to a set of five coupled linear algebraic equations. A solution requires the determinant to be zero. Because there are three prognostic variables this determinant is a cubic polynomial in the frequency ω. The existence of three roots corresponds to there being three independent modes of motion.

Two of the roots give the dispersion relation for internal waves:

$$\omega_s = s\left[\frac{N^2 k_h^2 + f^2 k_z^2}{k_h^2 + k_z^2}\right]^{1/2} \qquad s = +, - \tag{A5}$$

where k_h is the horizontal part of the wave vector $\mathbf{k}$. The third root is $\omega = 0$ (on the f-plane).

In the linear theory the internal wave variables at a given wave vector are related by

$$\begin{bmatrix} \xi \\ u \\ v \end{bmatrix} = \begin{bmatrix} -ik_h{}^2 \\ (\omega_s k_x + if k_y)k_z \\ (\omega_s k_y - if k_x)k_z \end{bmatrix} b_{\mathbf{k}} e^{i(\mathbf{k}\cdot\mathbf{x}-\omega_s t)} \qquad \text{(A6)}$$

where $b_{\mathbf{k}}$ is a complex amplitude. The fluctuating part of the potential vorticity, $\pi = \mathrm{PV} - f$, is

$$\pi = ik_x v - ik_y u - ik_z f\xi = 0. \qquad \text{(A7)}$$

It is the vanishing of potential vorticity, as well as the dispersion relation, which characterizes internal waves.

The potential vorticity containing motion has variables at a given wave vector related by

$$\begin{bmatrix} \xi \\ u \\ v \end{bmatrix} = \begin{bmatrix} -(f/N^2)k_z \\ -k_y \\ k_x \end{bmatrix} c_{\mathbf{k}} e^{i\mathbf{k}\cdot\mathbf{x}} \qquad \text{(A8)}$$

and the potential vorticity is

$$\pi = i\left[k_h{}^2 + \frac{f^2}{N^2} k_z{}^2\right] c_{\mathbf{k}} e^{i\mathbf{k}\cdot\mathbf{x}} \qquad \text{(A9)}$$

The three amplitude relations (A6) and (A8) represent a complete set of basis vectors in (u, v, ξ)—space and can be used to uniquely decompose any observed field into its internal gravity and its vortical mode component.

APPENDIX B

The GM 76 Spectrum

The Garrett and Munk (1972, 1975) internal wave model spectra have been changed and improved in the course of time. The version that is used in this paper is generally referred to as the GM 76 spectrum (Cairns and Williams, 1976). For this spectrum the distribution of total internal wave energy in frequency–horizontal wavenumber space is given by

$$E(\omega, \alpha) = b^2 N N_0 E_0 B(\omega) \frac{A(\alpha/\alpha_*)}{\alpha_*} \qquad \text{(B1)}$$

with

$$B(\omega) = \frac{2}{\pi}\frac{f}{\omega}(\omega^2 - f^2)^{-1/2} \qquad \text{(B2)}$$

$$A(\lambda) = \frac{2}{\pi}(1 + \lambda^2)^{-1} \qquad \text{(B3)}$$

$$\alpha_*(\omega) = (\omega^2 - f^2)^{1/2} N^{-1} \beta_* \qquad \text{(B4)}$$

$$\beta_* = \frac{\pi}{b}\frac{N}{N_0} j_*. \qquad \text{(B5)}$$

The parameters are chosen to be $b = 1.3 \times 10^3$ m, $N_0 = 5.2\ 10^{-3}\ \mathrm{s}^{-1}$, $E_0 = 6 \times 10^{-5}$ and $j_* = 3$. The spectrum also includes a high wavenumber cutoff

$$\alpha_c(\omega) = (\omega^2 - f^2)^{1/2}(N^2 - \omega^2)^{-1/2}\beta_c \qquad \text{(B6)}$$

with $\beta_c = 2\pi/10\ \mathrm{m}^{-1}$.

REFERENCES

Briscoe, M. G., 1975: Preliminary results from the trimoored internal wave experiment (IWEX). *J. Geophys. Res.*, **80,** 3872–3884.

——, 1977: On current finestructure and moored current meter measurements of internal waves. *Deep-Sea Res.*, **24,** 1121–1131.

Cairns, J. L., and G. D. Williams, 1976: Internal wave observations from a midwater float, Part II. *J. Geophys. Res.*, **81,** 1943–1950.

Dugan, J. P., 1984: Towed observations of internal waves and patches of fine-scale activity. Internal Gravity Waves and Small-Scale Turbulence. *Proc. Aha Huliko'a Hawaiian Winter Workshop,* Hawaii Inst. Geophys. Spec. Pub., P. Müller and R. Pujalet, Eds.

Eriksen, C. C., 1978: Measurements and models of finestructure, internal gravity waves, and wave breaking in the deep ocean. *J. Geophys. Res.*, **83,** 2989–3009.

Ertel, H., 1942: Ein neuer hydrodynamischer Wirbelsatz. *Meteorol. Z.*, **59,** 277–281.

Gage, K. S., 1979: Evidence for a K − 5/3 law inertial range in mesoscale two-dimensional turbulence. *J. Atmos. Sci.*, **36,** 1950–1954.

Gargett, A. E., P. J. Hendricks, T. B. Sanford, T. R. Osborne and A. J. Williams III, 1981: A composite spectrum of vertical shear in the upper ocean. *J. Phys. Oceanogr.*, **11,** 1258–1271.

Garrett, C. J. R., and W. H. Munk, 1972: Space-time scales of internal waves: A progress report. *Geophys. Fluid Dyn.*, **2,** 225–264.

——, and ——, 1975: Space-time scales of internal waves: A progress report. *J. Geophys. Res.*, **80,** 291–297.

Gregg, M. C., 1977: A comparison of finestructure spectra from the main thermocline. *J. Phys. Oceanogr.*, **7,** 33–40.

Henyey, F. S., 1983: Hamiltonian description of stratified fluid dynamics. *Phys. Fluids,* **26,** 40–47.

Holloway, G., 1981: Theoretical approaches to interactions among internal waves, turbulence and finestructure. *Conf. Proc., Nonlinear Properties of Internal Waves,* Amer. Inst. Phys., B. J. West, Ed., **76,** 47–77.

——, 1983: A conjecture relating oceanic internal waves and small-scale processes. *Atmosphere; Atmos. Ocean,* **21,** 107–122.

Joyce, T. M., and Y. J. F. Desaubies, 1977: Discrimination between internal waves and temperature finestructure. *J. Phys. Oceanogr.*, **7,** 22–32.

Lilly, D. K., 1983: Stratified turbulence and the mesoscale variability of the atmosphere. *J. Atmos. Sci.*, **40,** 747–761.

McKean, R. S., 1974: Interpretation of internal wave measurements in the presence of fine-structure. *J. Phys. Oceanogr.*, **4,** 200–213.

Müller, P., 1984: Small-scale vortical motions. *Internal Gravity Waves and Small-Scale Turbulence. Proc., 'Aha Huliko'a Hawaiian Winter Workshop,* Hawaii Institute of Geophys., Spec. Pub., P. Müller and R. Pujalet, Eds.

——, D. Olbers and J. Willebrand, 1978: The IWEX spectrum. *J. Geophys. Res.*, **83,** 479–500.

——, G. Holloway, F. Henyey and N. Pomphrey, 1986: Nonlinear interactions among internal gravity waves. *Rev. Geophys. Space Phys.* **24,** 493–536.

Munk, W. H., 1981: Internal waves and small scale processes. *Evolution of Physical Oceanography,* B. A. Warren and C. Wunsch, Eds., The MIT Press, 264–291.

Pinkel, R., 1985: The wavenumber-frequency spectrum of upper ocean shear. *J. Phys. Oceanogr.*, **15,** 1453–1469.

——, A. Plueddemann and R. Williams, 1987: *Preprints Internal Wave Observations From Flip in Mildex. J. Phys. Oceanogr.,* **17,** 1737–1757.

Riley, J. J., R. W. Metcalfe and M. A. Weissman, 1981: Direct numerical simulations of homogeneous turbulence in density-stratified fluids. Nonlinear Properties of Internal Waves, B. J. West, Ed., *Amer. Institute of Phys.*, **76,** 79–112.

VanZandt, T. E., 1982: A universal spectrum of buoyancy waves in the atmosphere. *Geophys. Res. Lett.*, **9,** 575–578.

Williams, R., and P. Müller, 1986: Potential vorticity estimates at small scales in the ocean. Rep. HIG-86-1, Hawaii Institute of Geophys., 99 pp.